

Sensitivity analysis of orbital motion around 2016 HO3 to the uncertainties of gravity and solar radiation pressure

Jinglang Feng¹, Xiyun Hou², Daniele Antonio Santeramo³, Pierluigi Di Lizia⁴, Roberto Armellin⁵

1 University of Strathclyde, United Kingdom, fjlangabc@gmail.com

2 Nanjing University, China, silence@nju.edu.cn

3 Politecnico di Milano, Italy, danieleantonio.santeramo@polimi.it

4 Politecnico di Milano, Italy, pierluigi.dilizia@polimi.it

5 ISAE-Supaero University of Toulouse, France, r.armellin@isae-superaero.fr

Abstract

For robust mission design, this study investigates the robustness of orbital motion in the vicinity of asteroid 2016 HO3 considering the uncertainties of the central gravity of HO3 and the solar radiation pressure (SRP). By applying the automatic domain splitting (ADS) algorithm, these uncertainties are propagated along the orbital motion and their effects on orbits with different geometries are investigated by evaluating the first split time of the orbits. Moreover, the number of splits and bounds of the state flow are also evaluated along the propagation as another criteria of indicating motion robustness and practical stability. The polar orbits are discovered to be more robust than the equatorial motion and other inclined motion. Specifically, the solar terminator orbit (STO) is bounded within a small range and is found to have the best robustness among all the polar motions, which can be used for practical mission purpose. The results are validated against numerical simulations and prove that robust motion exists even for very small bodies with weak gravity field. Therefore, this work contributes to systematically identify the robust motion near an asteroid considering the gravity uncertainty and the SRP perturbation for real mission operations from a new perspective.

Keywords: asteroid 2016 HO3, gravity uncertainty, automatic domain splitting, uncertainty propagation, robustness

1 Introduction

Small solar system bodies have become the popular targets of deep space missions, due to their scientific, technical and natural resources values. The recent and future missions include JAXA's Hayabusha2 to asteroid Ryugu [1], NASA's OSIRIS-Rex to Bennu [2], NASA's DART mission [3] and ESA's HERA mission [4] both to binary asteroid Dydimos. China is also planning its first asteroid mission and 2016 HO3 is a potential target [5]. 2016 HO3 is currently the smallest and closest quasi-satellite of Earth [6] with a diameter of about 40 m and resultantly very weak gravity. However, due to the limitations of ground observations, its gravity was determined with large uncertainty before the spacecraft's arrival, which brings about inaccurate design and prediction of mission orbits. As a result of the weak gravity of HO3, the solar radiation pressure (SRP) is an important perturbation on the orbital motion around HO3 and it should be considered in the dynamics. Moreover, the SRP cannot also be accurately determined as a result of the non-complete understanding of the reflection property of all the surfaces of the spacecraft. Therefore, considering these uncertainties and identifying the robust region of motion in the vicinity of asteroid 2016 HO3 are significant for real mission design.

There are various methods of propagating uncertainty, including using the linearized dynamics and the non-linear dynamics, respectively. For the former situation, the state transition matrix (STM) that transforms the deviation of the initial state to that of the final state of a trajectory is usually applied. And the eigenvalues and eigenvectors of this STM evaluates the evolution of the deviation of the initial state along with time, which also indicates the linear stability of this trajectory [7]. For the latter

situation, the MC method is a commonly used one by performing point-wise numerical simulations of the fully non-linear dynamics, which provides statistics of the true trajectory. However, it is computationally intensive and the time consumption increases with the increasing number of samples [8]. By approximating the initial arbitrary distribution with a limited number of samples, with a finite sum of weighted Gaussian distributions and with polynomial series, respectively, the unscented transformation (UT) [9], the Gaussian mixtures model (GMM) [10] and the polynomial chaos expansion (PCE) [11] have been developed to address the deficiency of the linearization. They are classified as non-intrusive methods since they do not require access to the dynamical equations and treat them as a black box. Alternative way to deal with the nonlinearity is based on approximation of the flow of the dynamics in Taylor or polynomial series, which requires the dynamical equations of the system and is categorized as the intrusive methods. Compared with MC and non-intrusive methods, they are more straightforward to capture the dynamical structure of the system. The general polynomial algebra (GPA) was recently developed to approximate the flow of the dynamics in multivariate and generic polynomial expansions [12]. It demonstrated good performance of propagating uncertainty sets through nonlinear dynamical systems. The differential algebra (DA) method performs Taylor expansion of the flow of the dynamics up to arbitrary order with automatic differentiation [13]. The final output of DA is a list of final state polynomials, each describing the evolution of the initial condition i.e. mapping the entire initial domain into the final set. Moreover, instead of running thousands of pointwise integrations of the Monte Carlo method, the integrations of DA are performed by the fast evaluation of the Taylor polynomials that is just algebra operations. Resultantly, the computational time is reduced considerably, while the accuracy can be kept arbitrarily high by adjusting the truncation order of the Taylor expansion. DA has been applied widely in the field of orbital dynamics, e.g. asteroid encounter analysis [14] and orbit conjunction analysis [15].

There has been extensive research about the dynamics and stability of orbital motion around small solar system bodies with deterministic models [16]. However, there are very limited studies about addressing the effects of uncertainties of either the gravity and the SRP on the dynamics or robustness of motion around small bodies. Taking asteroid Itokawa as an example and using Monte Carlo (MC) simulation, Melman et al. [17] investigated the effects of its uncertain gravity on the evolution of the so-called solar terminator orbit (STO) whose orbital plane is perpendicular to the Sun-asteroid line [18]. And the STO was found to be more sensitive to this uncertainty if the gravity of the asteroid is weak. For small asteroid Bennu with weak gravity field, a frozen-STO was found to be more robust against the execution uncertainties or errors than a circular-STO [19], based on the averaged dynamics and MC simulations. Applying the DA method, Feng et al. [20] propagated the uncertainty of the irregular gravity field of asteroid Stein and investigated its effect on the orbits with different geometry. Retrograde orbits were found to have better robustness than prograde ones. Therefore, this study extends the previous research and focuses on investigating the effects of uncertainties of gravity and SRP on motions in large phase space, with no restriction on the small values of these uncertainties. Moreover, the dynamics of motion around small bodies with perturbations is highly nonlinear.

Nevertheless, DA fails when the high non-linearity of the dynamics, the large initial uncertainty set and long-term propagation prohibit good convergence of the Taylor expansion and a single Taylor expansion of the flow is not accurate enough to map the entire initial uncertain domain. To overcome these problems, automatic domain splitting (ADS) was generated by automatically splitting the initial uncertain domain into subdomains, over each of which a new Taylor expansion with good convergence is obtained [21]. ADS has been successfully applied to the propagation of the motion of asteroid Apophis considering its initial state uncertainty. The non-impact and close-encounter regions of its state space w.r.t Earth were identified and validated against point-wise simulations [21]. In addition, it was also demonstrated that ADS is capable of inferring the dynamical behavior of the system over the initial uncertainty domain through the resulting splitting structure at the end of the propagation. Specifically, the region of frequent splits corresponds to the region of strong nonlinearity of the dynamics, which is automatically identified during the implementation of this algorithm. More

details of ADS are given in the following section. There have been several indicators characterizing the dynamical structure of the system. For instance, the Lyapunov Characteristic Exponent (LCE) is obtained from the eigenvalues of the STM based on the linearized dynamics of an autonomous system [22]. The zero value of LCE indicates the neighboring of this trajectory is bounded and linearly stable, and the positive value of LCE implies the neighboring trajectory will deviate exponentially from the nominal one. The other one is the so-called Lagrangian Coherent Structure (LCS) [23]. It is defined from the Finite-time LCE that indicates the divergence rate of trajectories with neighbouring initial conditions. And it is defined as ridges of the Finite-time LCE field of a time-dependent system for a time interval, to characterize the coherent structure within system that partition the phase space. However, LCS is computationally intensive for system with dimension higher than four. And they are based on the deterministic dynamics. Therefore, ADS could be served as the indicator of the dynamical structure of a highly nonlinear system with uncertainties, in terms of robustness and bounded motion etc., which is explored in this study.

Since HO3 is very small and has very weak gravity field, only the uncertainty of its central gravity is considered and the even weaker irregular gravity field is neglected. Therefore, taking into account the uncertainties of both the central gravity and the SRP, this study is organized as follows. Section 2 introduces the details of the ADS algorithm. Section 3 gives the dynamical model of orbital motion around HO3 and compares the magnitude of different perturbations to that of the central gravity. Section 4 applies the ADS algorithm to propagate the uncertainties and to investigate the sensitivity of orbital geometry (e.g. semi-major axis a , inclination i , etc.) to the uncertainties of both the central gravity and the SRP by evaluating their first split time, and resultantly identify the robust region. The results are validated against numerical simulations. Section 5 concludes this study and gives prospects for future work.

2 The methodology of ADS

The main idea of ADS is to determine the time at which the flow expansion over a given initial set, by applying an automatic algorithm, is not capable of describing the dynamics with the required accuracy anymore. Once this situation is detected, the domain of the original polynomial expansion is divided along one of the expansion variables into two domains of the same size. Then, the dynamics is re-expanded around the new center points of the two domains, respectively, resulting in two separate polynomial expansions. Since the new expansions do not change the order, each of the new polynomials is identical to the original ones on its respective domain. This process is illustrated in Fig.1, in which the error is the truncation error measuring the difference between the $n+1$ times differentiable function and its Taylor expansion of order n , which is an absolute value. And the ϵ is the required accuracy. Following on such a split, the integration continues on each subdomain in the same manner until further splits are required or the final integration time is reached. The result is a list of Taylor expansions approximating the final state, each covering a subset of the domain of initial conditions.

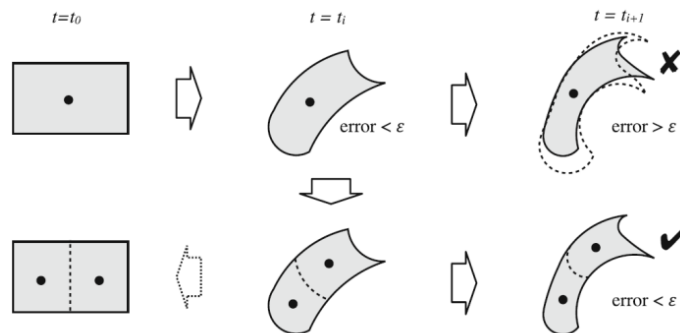


Figure 1 Illustration of the propagation process with ADS [21]

Specifically, all splits are performed in the direction of the variable that contributes the most to the truncation error of the polynomial, thus to maximize the reduction of the expansion error. During the splitting process, the split direction strongly depends on the parametrization of the initial condition and can occur automatically along all variables that contribute to the truncation error. However, the initial condition can be parametrized such that the expansion splits mainly along a few or even just one of the directions, corresponding to the variables that the dynamics is more sensitive to. In addition, the number of the maximum split times and the minimum domain size can be predefined and modified, according to the requirement on the efficiency and accuracy. It is pointed out here that it is possible that some subdomain cannot be mapped to the end of the integration due to the limitation on the minimum domain size. Moreover, it is also pointed out here that the earlier and the more times of the splits within a specific region occur, the stronger nonlinearity the dynamics is, as it is difficult to be managed with a single Taylor polynomial. The reader can refer to Wittig's paper [21] for more detailed description and demonstration about ADS.

3 Dynamical Modelling

The equation of motion for an object located at $\mathbf{r} = (x, y, z)$ in asteroid-centered inertial frame is given as

$$\ddot{\mathbf{r}} = \mathbf{F}_{acc} = -\frac{\mu}{r^3}\mathbf{r} + \mathbf{F}_{SRP} + \mathbf{F}_{third_body} \quad (1)$$

where the first term on the right-hand side of the equation is the acceleration from the central gravitational force and $\mu = Gm$ is the gravitational constant of the asteroid. The second term is the other perturbational forces from the SRP and the third body gravitation from Sun and Earth. For the cannonball model of the s/c, \mathbf{F}_{SRP} can be expressed as

$$\mathbf{F}_{SRP} = -(1 + \eta) \cdot \rho_0 \Delta_0^2 \cdot \frac{S}{m} \cdot \left(\frac{\Delta}{\Delta_0^3}\right) = -(1 + \eta) \cdot \rho_0 \cdot \frac{\Delta_0^2}{\Delta^2} \cdot \frac{S}{m} \cdot \left(\frac{\Delta}{\Delta_0}\right)$$

in which η is the reflection coefficient of the s/c and $\eta = 1$ is for full reflection, $\frac{S}{m}$ is the area to mass ratio of the s/c, ρ_0 is the solar radiation flux at the reference distance Δ_0 (e.g. $\rho_0 = 4.56 \times 10^{-6}$ at distance of 1AU). And $\Delta = \mathbf{r}_{\odot} - \mathbf{r}$ is the relative position vector of the Sun to the s/c, as indicated in Fig.2.

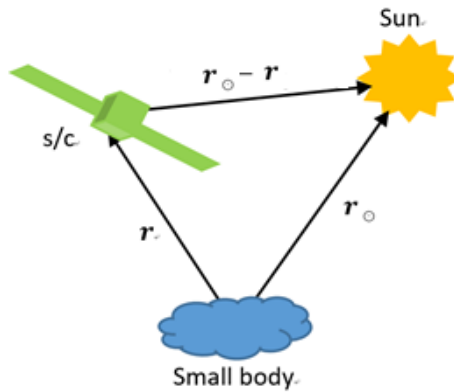


Figure 2 Illustration of the geometry of the s/c and Sun in the asteroid-centered inertial frame.

The third body acceleration \mathbf{F}_{third_body} is given as

$$\mathbf{F}_{third_body} = -GM \left(\frac{\mathbf{r}_{\odot}}{r_{\odot}^3} - \frac{\mathbf{\Delta}}{\Delta^3} \right)$$

in which GM is the gravitational constant of the third body.

For the convenience of following numerical simulations, this dynamical system is normalized with the unit of mass, length and time defined as

$$[M] = m_{HO3}, [L] = R_{HO3}, [T] = \sqrt{\frac{[L]^3}{G[m]}}$$

Therefore, the relationship between the normalized and the original accelerations can be obtained as

$$[a] = \frac{d^2 r}{d\tau^2} = \frac{d^2 \frac{R}{[L]}}{d \left(\frac{t}{[T]} \right)^2} = \frac{[T]^2}{[L]} \cdot \frac{d^2 R}{dt^2} = \frac{[T]^2}{[L]} \cdot a$$

Given the area to mass ratio and reflection coefficient of the s/c as $0.02 \text{ m}^2/\text{kg}$ and 0.4 , respectively, the evolution of the magnitudes of the normalized forces on the s/c around HO3 with the normalized distance to HO3 is given in Fig.3.

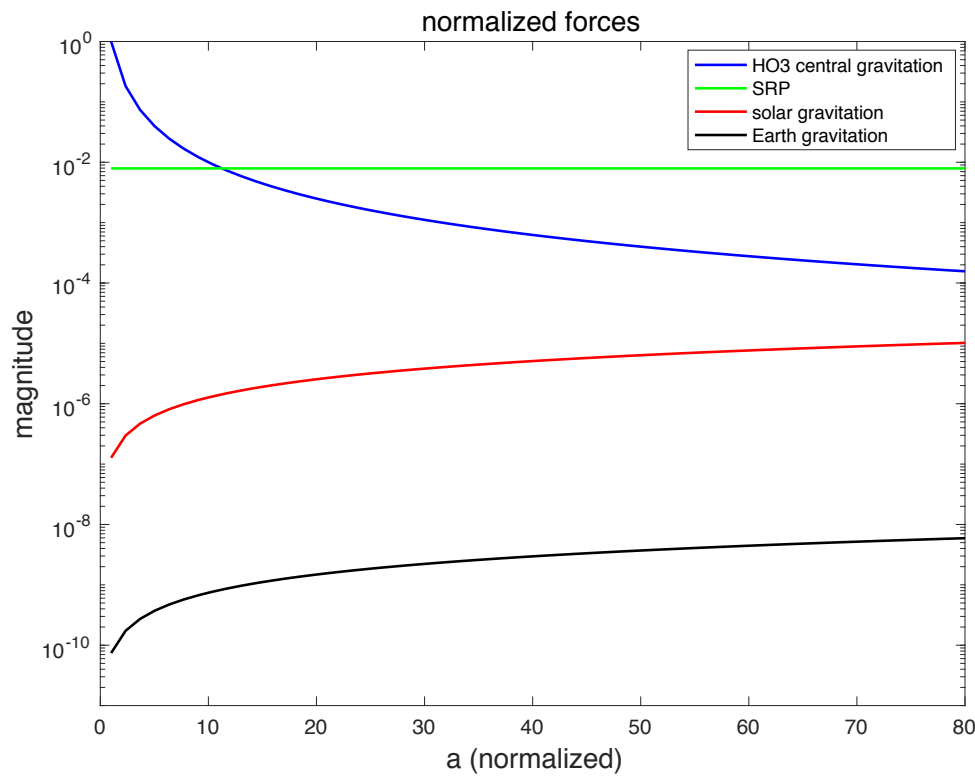


Figure 3 The magnitudes of the normalized forces at different distances to HO3.

It can be seen that SRP is the dominant perturbation and becomes even larger than the central gravitation of HO3 when the orbital altitude approximately exceeds ten times reference radius of HO3. The magnitudes of the solar gravitation and Earth gravitation are generally 4 or 5 and 7 or 8 orders smaller than that of the SRP, respectively. Therefore, the central gravitation, SRP and solar gravitation are the forces considered in the following simulations, and the Earth gravitation is ignored.

Since the DA-based ADS method is used to obtain the high order expansion of the state flow w.r.t the uncertain parameters that are denoted as \mathbf{p} . The first step is to initialize \mathbf{p} as a DA variable

$$[\mathbf{p}] = \mathbf{p} + \delta\mathbf{p}$$

where $\delta\mathbf{p}$ represents the displacement from the nominal value of \mathbf{p} . As discussed in the introduction, both the uncertainties of the central gravitation and the SRP are considered. Therefore, the uncertain parameter vector is specified as $\mathbf{p}_0 = (\mu, F_{SRP})$ and $\delta\mathbf{p}_0 = (\delta\mu, \delta F_{SRP})$, and the μ and F_{SRP} terms are expressed as DA variables as

$$\begin{cases} [\mu] = \mu + \delta\mu \\ [F_{SRP}] = F_{SRP} + \delta F_{SRP} \end{cases}$$

Therefore, as a demonstration, the corresponding first-order expansion of the dynamics defined in Eq.(1) is given as

$$\ddot{\mathbf{r}} = \mathbf{F}_{acc} \approx \mathbf{F}_{acc_\mu} \cdot \delta\mu + \mathbf{F}_{acc_SRP} \cdot \delta F_{SRP}$$

in which \mathbf{F}_{acc_μ} and \mathbf{F}_{acc_SRP} are the derivatives of the total acceleration force \mathbf{F}_{acc} w.r.t μ and F_{SRP} , respectively. And the high-order expansions are obtained based on auto-differentiation.

4 Numerical Simulations

4.1 The uncertainties of central gravity μ and SRP

The heliocentric orbit elements of HO3 is given in Tab.1 and is used in the following simulations. According to [24], the best global Gm or μ solution of HO3 can be determined to be $4.9781 \times 10^{-11} \pm 1.1378 \times 10^{-12} \text{ km}^3/\text{s}^2$, with the 3σ error of 2.29%. Since the uncertainty of the SRP is related to the shape and different materials of the s/c, its 1σ value σ_{SRP} is set to be 8×10^{-5} , corresponding to about 1% of the normalized SRP.

Table 1 Heliocentric Keplerian orbital elements of (469219) 2016 HO3 at epoch JD 2457600.5 that corresponds 2016 July 31 (J2000.0 ecliptic and equinox) [24]

semimajor axis a (au)	1.001229935	ascending node Ω ($^\circ$)	66.51326
eccentricity e	0.1041429	perihelion ω ($^\circ$)	307.22765
inclination i ($^\circ$)	7.77140	mean anomaly M ($^\circ$)	297.53211

Before proceeding to the systematic simulations, the relation between the expansion order and computational time consumption for different precisions is given in Fig.4, using the example orbit with semi-major axis value of 1.4 and all other orbital elements set to zero for the time interval of 40. And the 1σ values of uncertainties of μ and the SRP are 0.76% and 1%, respectively. It can be seen that for the same precision the 6th-order expansion generally requires more computational time than these of the other higher orders, due to the fact that the low-order expansion requires more splits and resultantly more computational time. For the 8th-order expansion, it needs slightly more computational time the 10th-order expansion, except for the precision of 1×10^{-9} . This phenomenon is caused by the interactions among the expansion order, number of splits and the time interval of the integration. For this research, the expansion order of 8 and the error tolerance or precision ε of 1×10^{-8} is a good balance of both efficiency (computation time) and accuracy (evidence) and is selected for the following simulations.

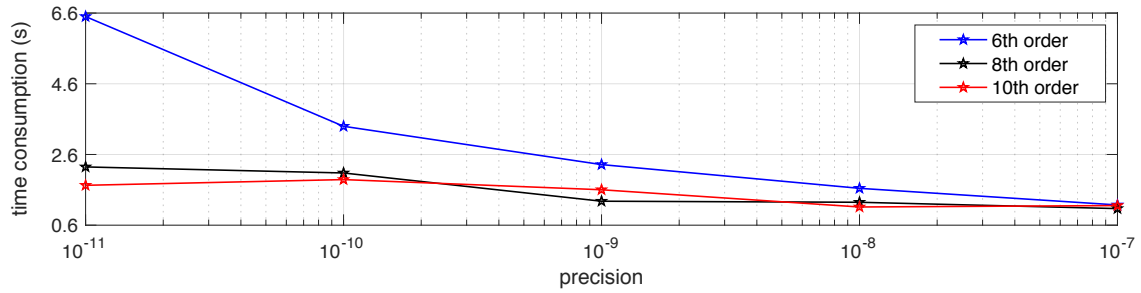
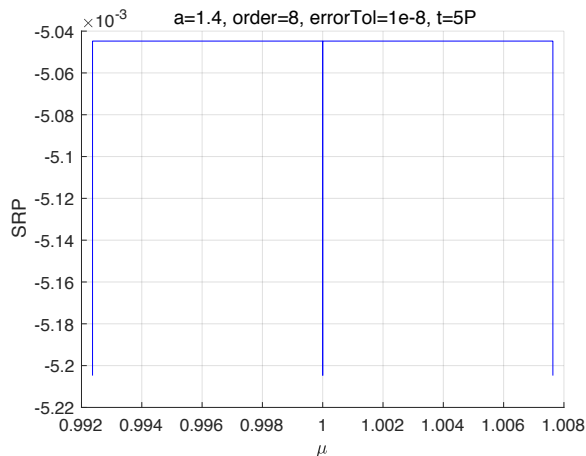


Figure 4 The relation between the expansion order and time consumption for different precisions.

4.2 Domain Split on the μ -SRP plane

In this section, by varying the semi-major axis and propagation time of the orbital motion, the split of the initial uncertain domain on the μ -SRP plane is investigated to identify the sensitivity of the dynamics on the uncertainties of μ and the SRP, respectively. Given the nominal values of μ and SRP, the motion will escape rapidly for the semi-major axis larger than 4.76, which is estimated by the formula $\sqrt{3\mu/16a_{SRP}}$ given in [16]. Therefore, this paper focuses on the orbital motion with a no larger than this value.

For the numerical simulation, the semi-major axis a with values of 1.4, 2.5, and 3.5 are selected. All the other orbital elements are set to zero. Specifically, the initial eccentricity is set to zero as the circular orbit is more proper for mission operation. And the initial inclination is set to zero as the prograde orbit is generally very unstable and is prone to split. The time interval of integration is firstly set to be five orbital period for each orbit, corresponding to the actual simulation time of 26, 62, 103, respectively. Their split of domain on the μ -SRP plane is given in Fig.5 and the number of splits are 1, 26 and 335, respectively. When the value of a increases from 1.4 to 3.5, more splits occur in the μ direction mainly due to the accumulation of the truncation error of Taylor expansion along with time. In the SRP direction, the domain starts splitting for $a = 2.5$ and the splits number increases significantly for $a = 3.5$, because with the increase of the semi-major axis the SRP plays an increasingly significant role and the effect of central gravitation gradually recedes.



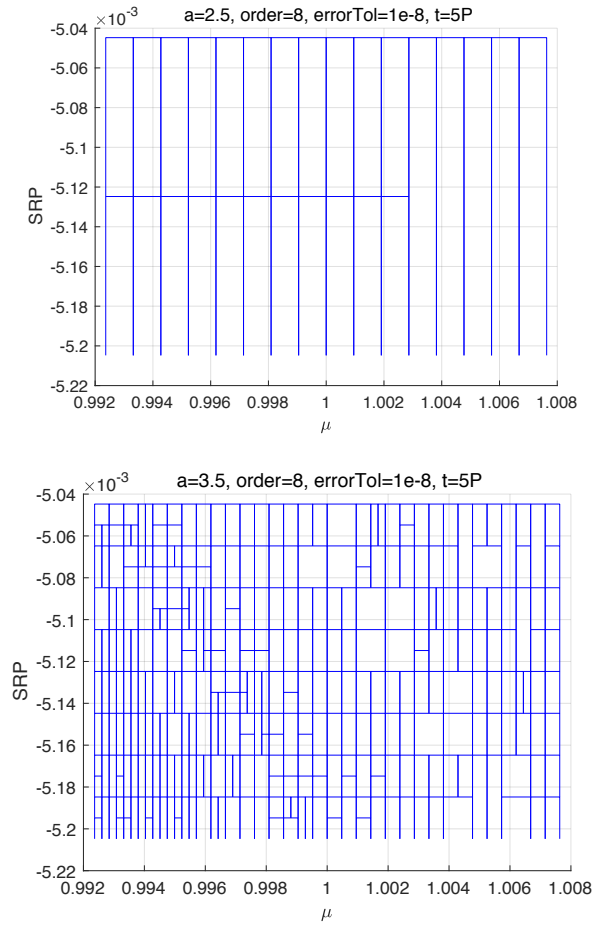


Figure 5 The domain split on the μ -SRP plane for $a = 1.4, 2.5, 3.5$ with the integration time of five orbital periods for each of them.



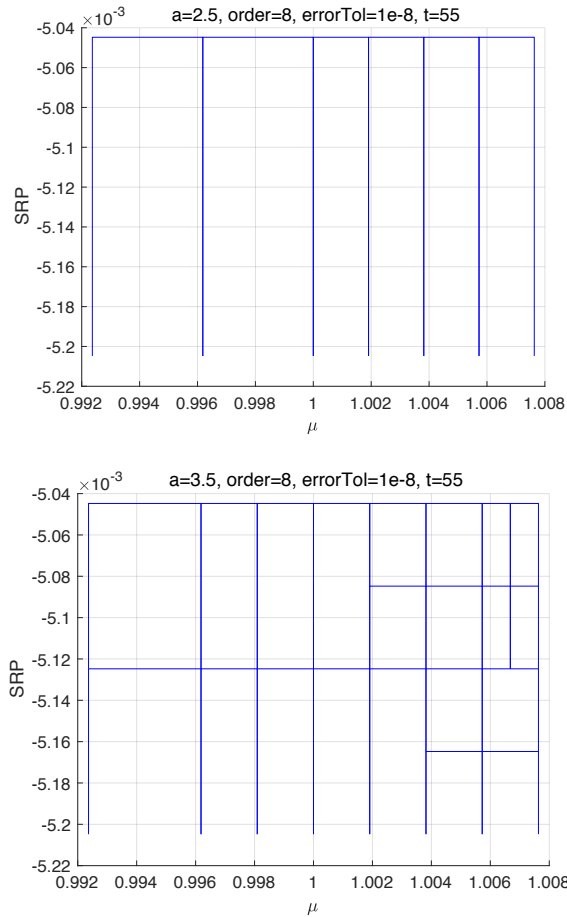


Figure 6 The domain split on the μ -SRP plane for $a = 1.4, 2.5, 3.5$ with the integration time of 55 for all of them.

In addition, for direct comparison, the same time interval of integration 55 is applied to all the three orbits and the domain split is given in Fig.6. It can be seen that the orbit with $a = 1.5$ has the most splits along the μ axis, indicating that the low-altitude motion is most sensitive to uncertain central gravitation. For the orbit with $a = 3.5$, the splits in the μ axis are obviously less but a few splits start appearing in the SRP direction due to the increasing influence of the SRP perturbation on high-altitude orbit. The domain splitting of the middle-altitude orbit with $a = 2.5$ is the transition between those of the other two orbits. This phenomenon is in line with the fact that the low-altitude motion is dominated by the central gravitation and the high-altitude more is more influenced by the SRP perturbation [16]. The middle-altitude motion is kind of a balance between the dynamics of the central gravitation and that of the SRP perturbation [16]. In summary, the number of split mainly depends on the perturbative or nonlinear dynamics and the integration time, both of which are closely related to the accuracy of the Taylor expansion. It also demonstrates that ADS is an indicator of the strong nonlinearity of the dynamics and sensitivities to the uncertain variables, and its role in identifying the region of robust motion will be discussed in the following section.

4.3 Sensitivity analysis and regions of robust motion

For the practical mission application, two kinds of orbital motion are mainly considered. The first one is the regular circular orbits (RCO), the orbital motion of which is possible only if the s/c is very close to HO3, and the RCO is obtained in the HO3-centered inertial frame. The second one is the solar terminated orbits (STO), a specific type of polar orbits that the precession rate of its orbital plane is the same as the rate of the mean orbital motion of the small body around Sun, i.e. its orbital plane always face Sun perpendicularly [16]. STO is preferred for the situation when the SRP perturbation is

strong. STO is obtained in the HO3-centered co-rotating frame that is coincide with the HO3-centered inertial frame at the initial epoch in this study. Its initial condition is transformed back to the HO3-centered inertial frame for the following numerical simulations.

4.3.1 Map of the first split time on the $a - i$ plane of RCO

To analyze the effects of the uncertain gravity field and SRP on orbits with different geometry, the circular orbits with different combinations of a and i are simulated. For a circular orbit, given the inclination i , the ascending node Ω and $u = \omega + f$ fully describe the orientation of this circular orbit and the position of the initial point on it, respectively. For the simulation in this section, Ω and u are both set to zero, and elements a and i are gridded within the range $a \in [1, 4]$, $i \in [0, 180^\circ]$. Since the uncertainty of the SRP is related to the shape and different materials of the s/c, its 1σ value σ_{SRP} is difficult to be determined accurately and therefore another value 8×10^{-4} (corresponding to about 10% of the normalized SRP) is also simulated in addition to the value 8×10^{-5} . For each orbit, the time epoch when the first split occurs is recorded and is normalized by the orbital period of this orbit. The corresponding map is generated on $a - i$ plane and is given in Fig.7.

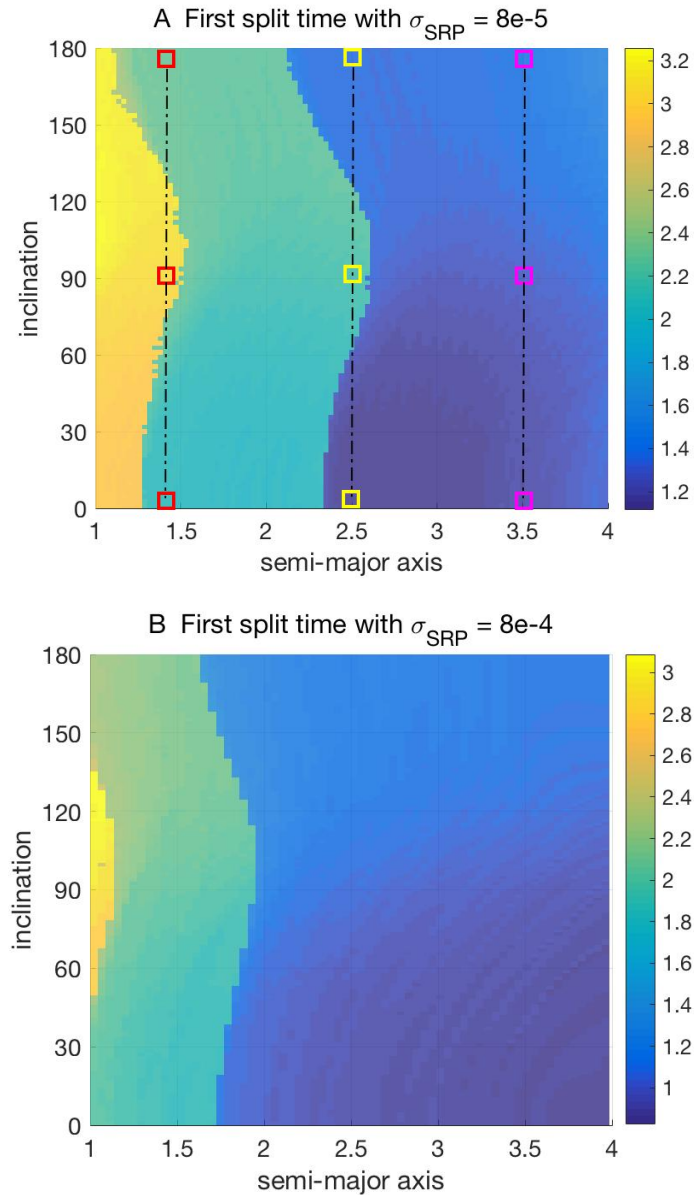
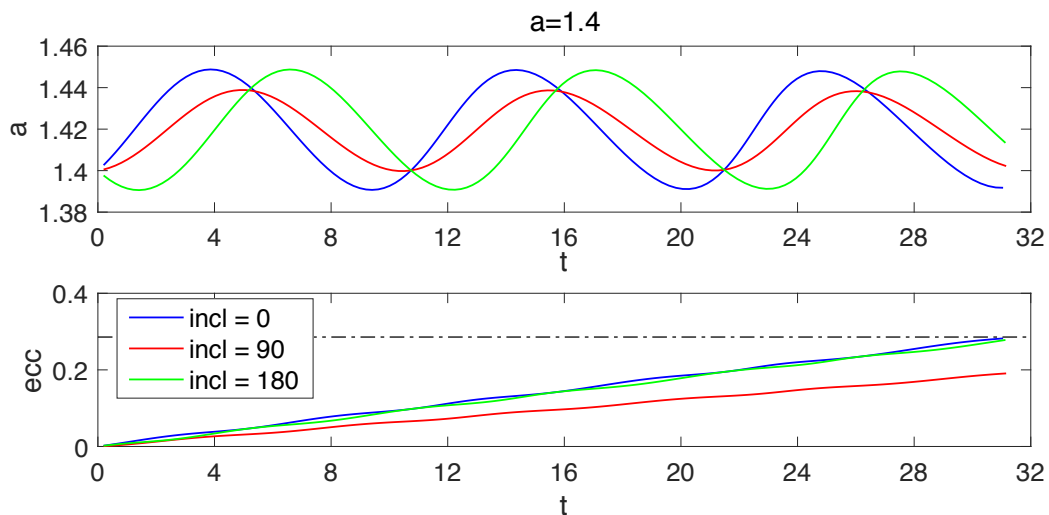


Figure 7 Map of the first split time normalized by its orbital period on $a - i$ plane for different values of σ_{SRP} .

It can be seen that the general structure of the two plots are similar, i.e. three apparent layers distributing along the semi-major axis direction. The yellow region (with the average first split time of about 3) is the most robust region (indicating by the firstly split time) located closest to the small body, due to the fact that the central gravitation of HO3 dominates the dynamics in its vicinity and the SRP plays the role of a small perturbation. When moving further away from HO3, the orbital motion becomes less robust as indicated by the light green region with the average first split time of about 2.2, when the central gravitation becomes weak and the SRP perturbation is stronger. Further away, there is a large blue area on the right most with the average first split time of about 1.4, where the motion is not robust due to the very strong SRP perturbation. Generally, when the orbit is far away from HO3, it becomes less robust. Nevertheless, the bump of each of the three regions indicates the near polar region is more robust against the SRP perturbation.

In addition to the similarities between Fig.7A and Fig.7B, the two plots also have obvious differences mainly on the location and size of the three regions. In Fig.6B, when the uncertainty value of the SRP is large, the yellow region is only restricted to the polar region and to the extremely close distance to HO3. However, for Fig.6A with the uncertainty value of the SRP ten times smaller than that of Fig.6B, the yellow region significantly extends to the regimes with both different inclinations and further distances. The light green region also expands obviously and the blue region shrinks correspondingly. These changes are due to the same reason that the motion becomes more robust when the uncertainty of the SRP reduces. In addition, for both Fig.6A and 6B, the lower half orbits split slightly before the upper half orbits, indicating the retrograde orbits are generally slightly more robust than these of the prograde ones. This phenomenon is actually weakened due to the relatively strong SRP perturbation w.r.t the weak gravity of HO3, though retrograde orbit is expected to be much more stable than the prograde ones [16]. Therefore, these comparisons indicate that the robustness of orbital motion is closely related both the dynamics and the uncertainties of the forces.

4.3.2 Numerical Integrations of the sample RCOs



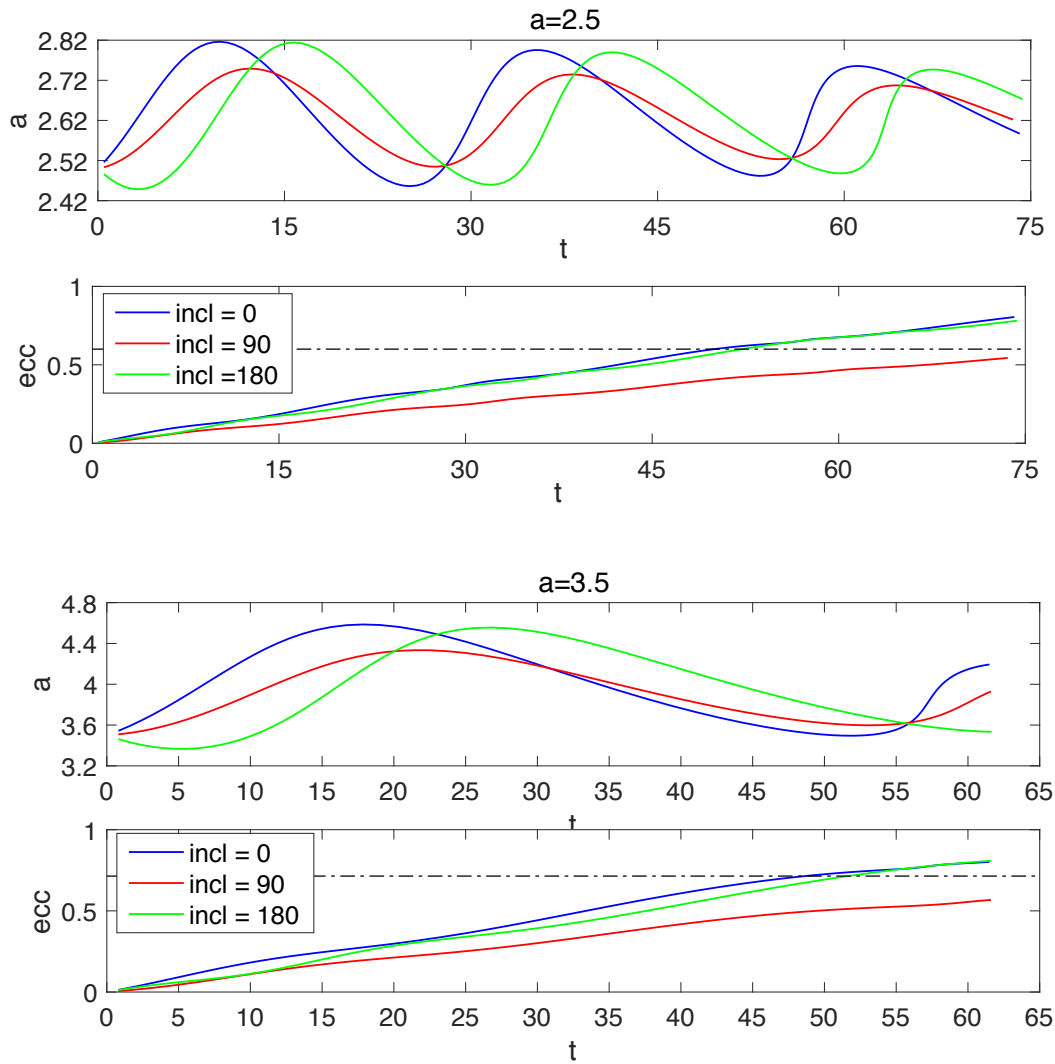


Figure 8 The evolutions of semi-major axis and eccentricity of the sample orbits from Fig.7A.

For a straightforward evaluation of the stability of the orbit motion, six sample orbits that are marked as squares are selected from Fig.7A for numerical integrations, i.e. orbits with $a = 1.4, 2.5, 3.5$ and $i = 0, 90, 180$ deg for each value of a with the integration time of $3P, 5P$ and $1.5P$, respectively. And their orbital evolutions are given in Fig.8. Since a, e and i are the most concerned orbital elements here and the orbit inclinations are found to have slight variations, only the evolutions of a and e are shown for each orbit. It can be seen that for the three different values of a , all the polar orbits that are indicated by the red lines have the smallest variational amplitudes in semi-major axis and also the smallest increasing rate of eccentricity, compared with these of the equatorial orbits with $i = 0$ and 180 deg. The black dash-dot lines in each evolutionary plot of e indicate the impact eccentricity for each specific value of a . Resultantly, non-polar orbits always reach this line much earlier than the polar orbits. It can be seen that the identified more robust motion is generally more stable or bounded than other motions, which can be defined as practical stability. The stability here is measured by the 'closeness' of the evolutionary trajectory to the initial or original trajectory. This definition is very useful or applicable to real mission operations where the free orbital motion (without maneuvers) that meet the accuracy requirements of observations for radio or laser tracking and navigation is preferable regardless of whether it's Lyapunov stable or not [25]. In fact, it was also discovered in our previous study about the motion around small bodies that the polar region is generally stable and the eccentricity can be stimulated to large value by the SRP even for equatorial orbits [26], which is currently proved by these numerical simulations. Moreover, for the equatorial orbits with $a =$

1.4, 2.5, 3.5, they can complete approximate three, two and one orbital revolution, respectively, before impacting on the small body. In addition, the amplitude of evolutions of the eccentricities of the green retrograde orbits are always slightly smaller than these of the blue prograde one. These phenomena also prove our previous interpretation that the yellow, light-green and blue regions in Fig.6 indicate the most, medium and least robust or practical stability of the motion, respectively. In summary, the map of the first split time provides an efficient indicator of robustness and practical stability considering modelling uncertainties.

4.3.3 The first split map on the $a - \Omega$ plane of Polar orbits and STO

Since the polar motion has been proven to be more robust than other non-polar ones, it is investigated in detail in this section. For polar orbits, as the ascending node Ω determines the orientation of the orbit in space, map of the first split time is generated on the $a - \Omega$ plane for sensitivity analysis. And the other orbital elements are set as $e = 0, \omega = 0$ deg, $i = 90$ deg with the σ_{SRP} uncertainty of the SRP at 8×10^{-5} and 8×10^{-4} , respectively.

In Fig.9A, for $\Omega < 90$ deg, the rectangular region consists of four different colour layers transiting from the yellow region in the upper left corner to the deep blue region in the lower right corner, i.e. from the most to the less robust motion. For $\Omega > 90$ deg, the structure of the map consists of three different colour layers transiting from the yellow region in the lower left corner to the deep blue region in the upper right corner, i.e. from the most to the less robust motion. For both Fig.9A and Fig.9B, the polar motion is shown to be more robust if it is closer to the smaller body or if it is closer to the region of $\Omega = 90$ deg that is demonstrated by the black dash-dot line for the same distance to the small body. The most robust region of $\Omega = 90$ deg corresponds to the terminator orbit, mainly due to the fact that this initial orbital geometry is less perturbed by the SRP as discussed at the beginning of Section 4.3. There are generally two types of STO, one kind that has been extensively studied is the circular STO with the initial condition given as

$$e_0 = 0, i_0 = \pi/2, \Omega_0 = \pi/2$$

The second type is the frozen STO with eccentricity and the perigee staying frozen, i.e. $\dot{e} = \dot{\omega} = 0$, and its initial condition is given as [16]

$$e_0 = \cos\Lambda, i_0 = \pi/2, \Omega_0 = \pm \pi/2, \omega_0 = \mp \pi/2$$

in which

$$\tan\Lambda = \frac{3}{2}(1 + \eta) \cdot P_{\odot} \cdot \frac{s}{m} \cdot \sqrt{\frac{a}{\mu\mu_s A(1 - E^2)}}$$

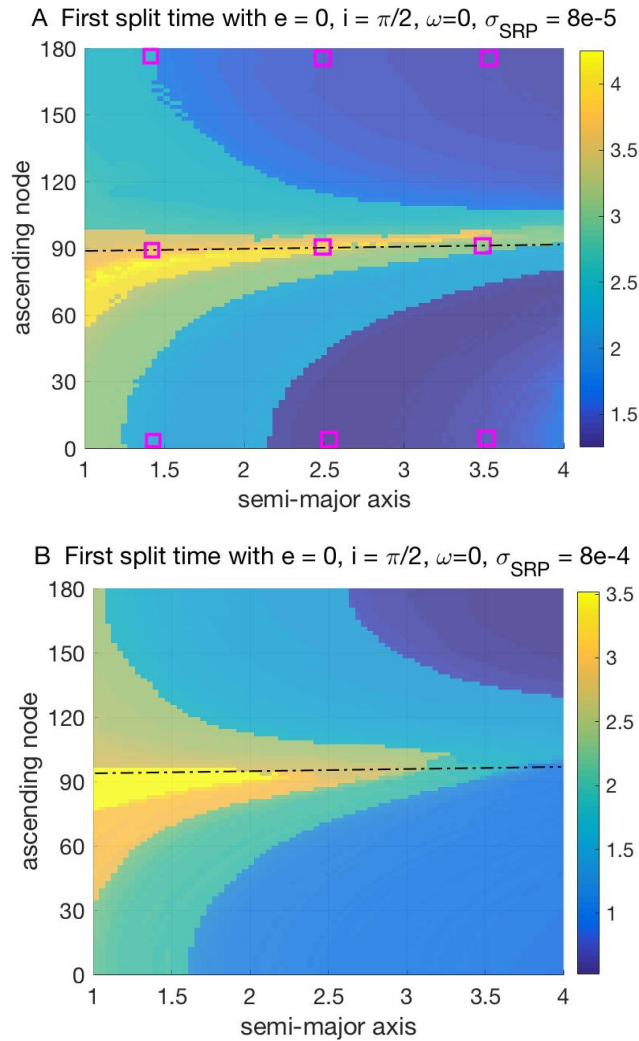


Figure 9 The first split time normalized by its orbital period on $a - \Omega$ plane for different σ_{SRP} .

where $P_{\odot} = 1 \times 10^8 \text{ kg} \cdot \text{km}^3 / (\text{s}^2 \cdot \text{m}^2)$ is the solar flux constant and a is the semi-major axis of the STO, A and E are the semi-major axis and eccentricity of HO3 around the Sun. Due to the weak gravitation of HO3, the frozen eccentricity e as a function of a is very small as shown in Fig.10. and therefore, the frozen STO is a near circular orbit for the scenario of HO3.

Again, we select several sample polar orbits from Fig.9A that are marked with rectangular, to simulate their orbital evolution for $a = 1.4, 2.5, 3.5$ and $\Omega = 0, 90, 180$ deg. And other orbital elements e, i are all fixed to zero and 90 deg, respectively. For $\Omega = 90$ deg, ω is set to 0 and -90 deg for the initial conditions of the circular and frozen STO, respectively. For other values of Ω , ω is all fixed to 0 for a generalized polar orbit.

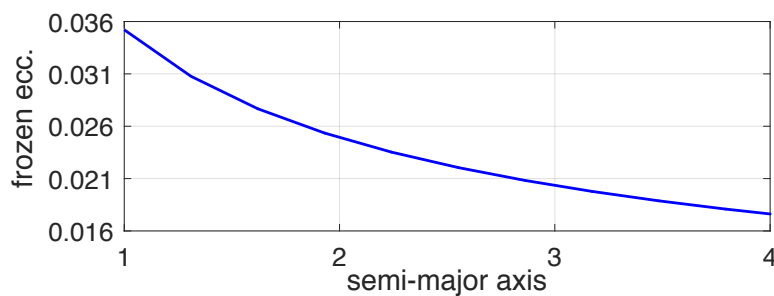
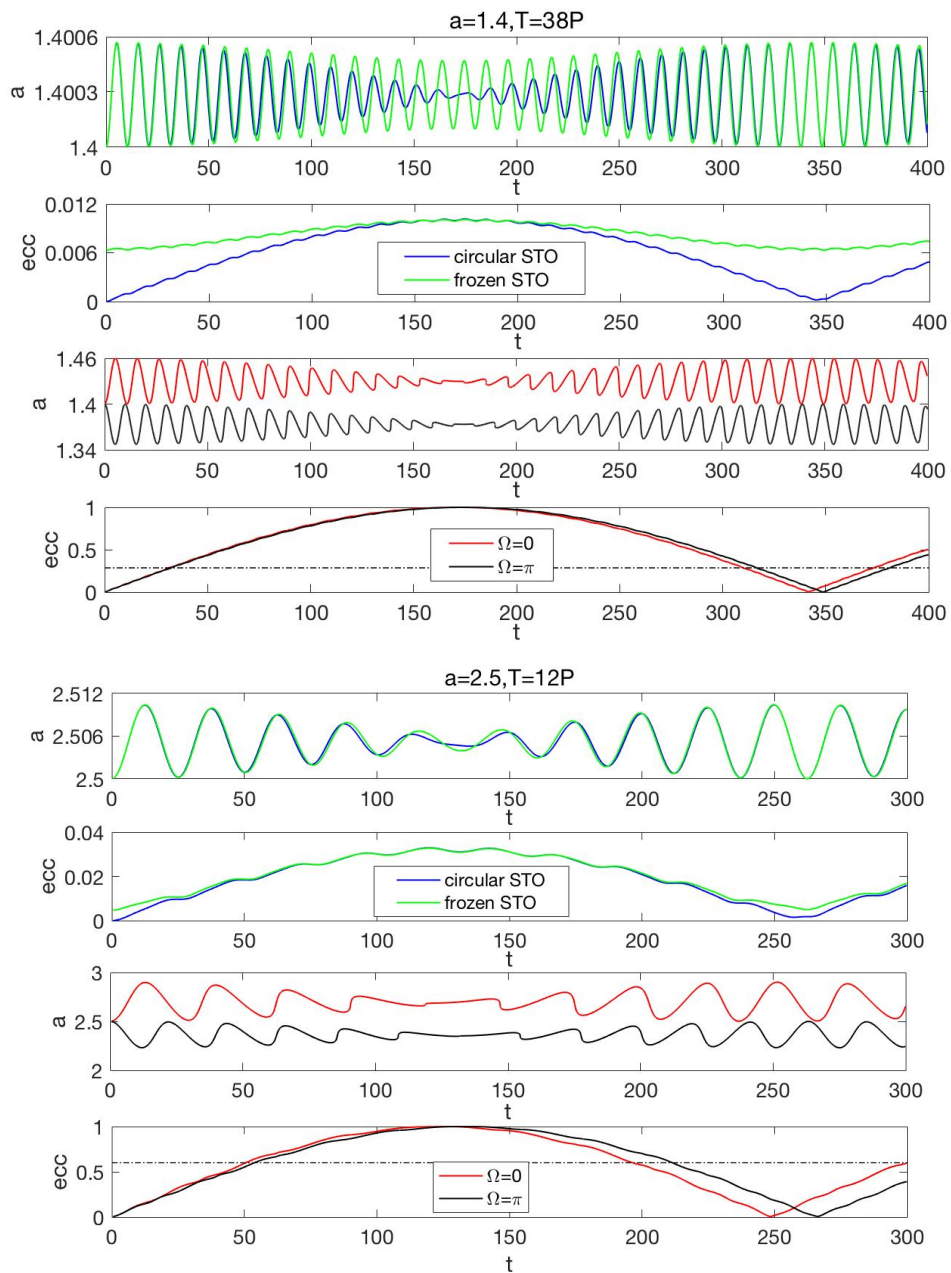


Figure 10 The eccentricity of a frozen STO at different semi-major axis



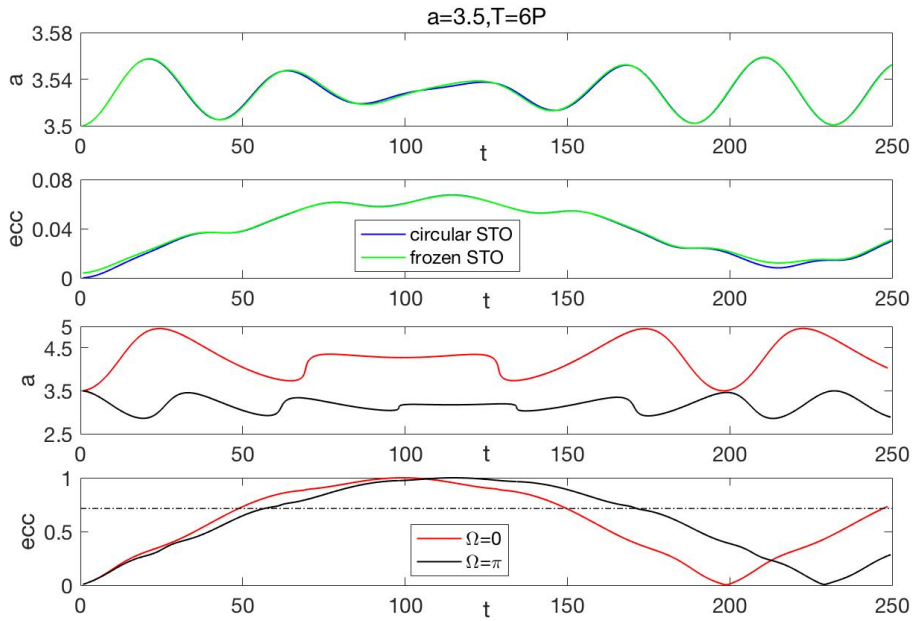


Figure 11 The evolutions of orbital elements a , e , ω of the sample orbits from Fig.8.

The evolutions of orbital elements a and e are given in Fig.11. It should be noticed that the duration of the simulations is different for $a = 1.4, 2.5, 3.5$, respectively, to capture the whole evolution process of each orbit. For all the sample orbits with $\Omega_0 = 90$ deg, i.e. the circular STO and frozen STO, they all have the smallest variations of both a and e , as indicated by the blue and green lines in the plots, respectively. Nevertheless, these orbits have long-term practical stability and stay well bounded, in terms of not impacting HO3 and the distance to HO3 not varying significantly. They are ideal candidates for orbits of mission operations. In addition, the circular STO performs slightly better than the frozen STO, especially for low-altitude motion. This is because the frozen STO is obtained from the averaged dynamics only accounting for the long-term and secular effects and neglecting the short-term effect embedded in the full dynamics, which cannot approximate the real dynamics accurately.

For sample orbits either with $\Omega_0 = 0$ (red line) or 180 deg (black line), their a and e have very large oscillations and after a short period of time their e reaches the impact eccentricity indicated by the black dash-dot line, which shows their strong instability. Moreover, the analysis of these simulations is consistent with the first split time obtained in Fig.9 as an indicator of robustness and also practical stability. Again, it proves that the ADS provides an efficient tool to measure the nonlinear dynamics and to indicate the robustness and practical stability through the first split map. An illustration of the sample orbits with $a = 2.5$ in three-dimensional inertial space is given in Fig.12 for the integration duration of $10P$. It can be seen that both the circular STO and frozen STO with $\Omega_0 = 90$ deg are well bounded within a relatively small region and the other two orbits spread extensively in their original orbital plane and vary far from the original orbits.

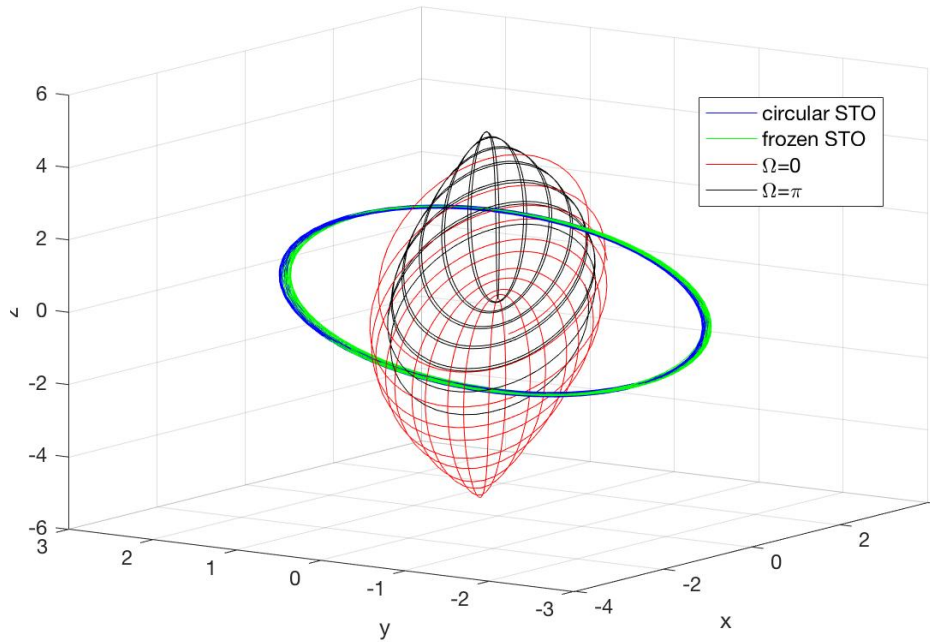


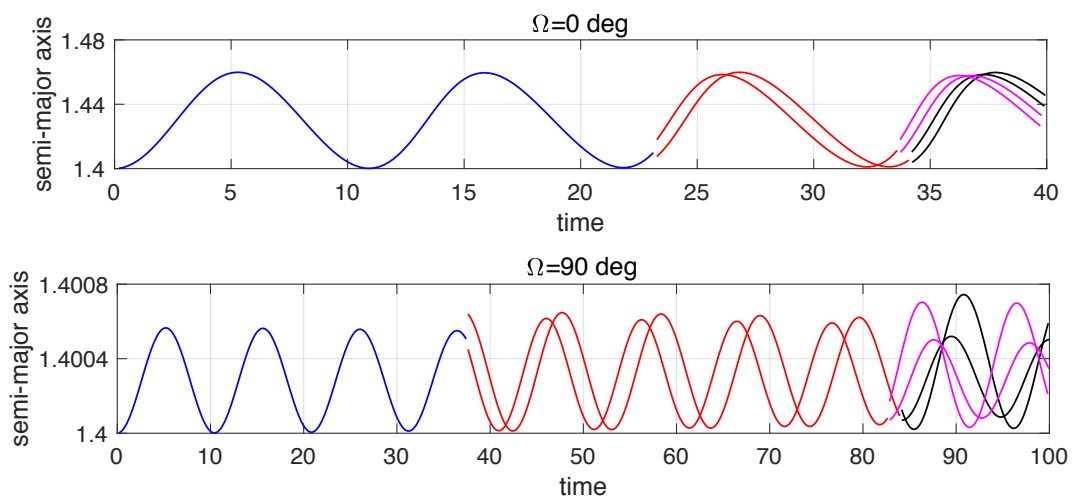
Figure 12 The numerical orbits in 3D space with $a = 2.5$ for the integration duration of 10P.

4.4 Split history and Bounds of the trajectory

Since the terminator orbits have been proven to be the most robust in the previous section, this section focuses on obtaining and analysing the split history and the bounds of the trajectory along their orbital evolution, due to the uncertainties of central gravitation and SRP (with 1σ uncertainty of 8×10^{-5}).

4.4.1 Split History of sample polar orbits

Taking the example orbits with $a = 1.4$, $i = 90$ deg, $e = 0$, $\omega = 0$ deg and for $\Omega_0 = 0$ and $\Omega_0 = 90$ deg, respectively, the evolutions of their a and e of both the center trajectory and the split trajectories are given in Fig.13, for comparison. For orbit with $\Omega_0 = 0$ deg, the first split occurs at about $t=23$ and the following-on splits occur at about $t=34$. These splits occur at earlier time epochs, compared with these of orbit with $\Omega_0 = 90$ deg at $t=37$ and $t=83$, respectively, which also indicates the robustness of the circular STO as discussed in the previous section.



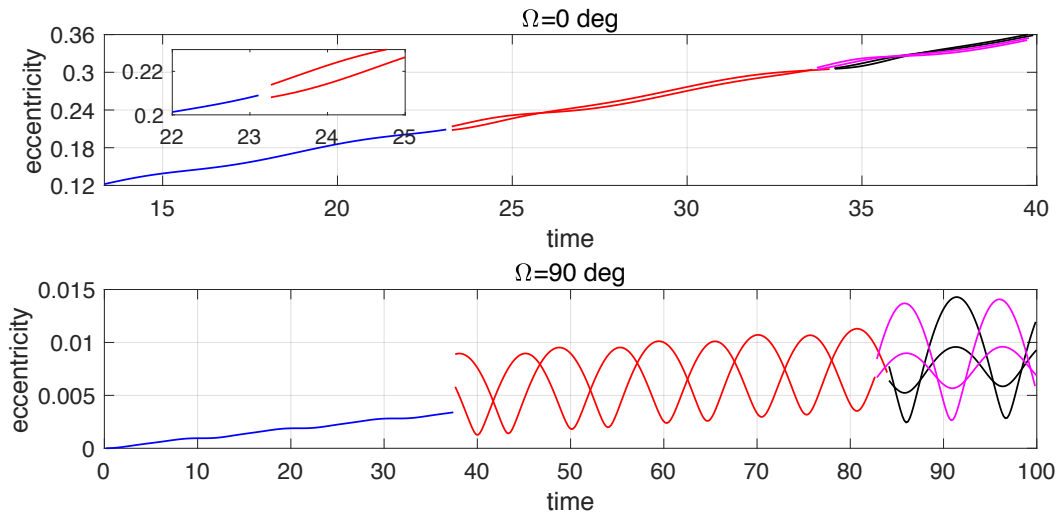


Figure 13 The split history of a and e for orbit with $a = 1.4$, and $\Omega_0 = 0$ and $\Omega_0 = 90$ deg.

4.4.2 The bounds of sample polar orbit

For $a = 1.4$, the evolution of the distance of the center trajectory (black line) and its bounds to HO3 (blue area) till the time epoch of the first split with $\Omega_0 = 0$ and $\Omega_0 = 90$ deg is given in Fig.14, respectively. For both orbits, the bounds are very narrow especially for $t < 5$, after which the bounds start expanding significantly and gradually with the accumulation of time. Since the distance of some of the lower bounds to HO3 already becomes smaller than one (the black dash-dot line), there is a possibility that the motion will impact on the body even before the eccentricity reaches the impact value, due to the uncertainties of the central gravity and SRP. In particular, for $\Omega_0 = 0$ deg and 90 deg, respectively, this might happen when t is at 23 and at 27, respectively. In addition, the distance of the center trajectory to HO3 (the black line) of orbit with $\Omega_0 = 0$ deg varies significantly than that of orbit with $\Omega_0 = 90$ deg, indicating again the better practical stability of circular STO. The evolution of bounds provides quantitative information for designing robust navigation and control algorithms.

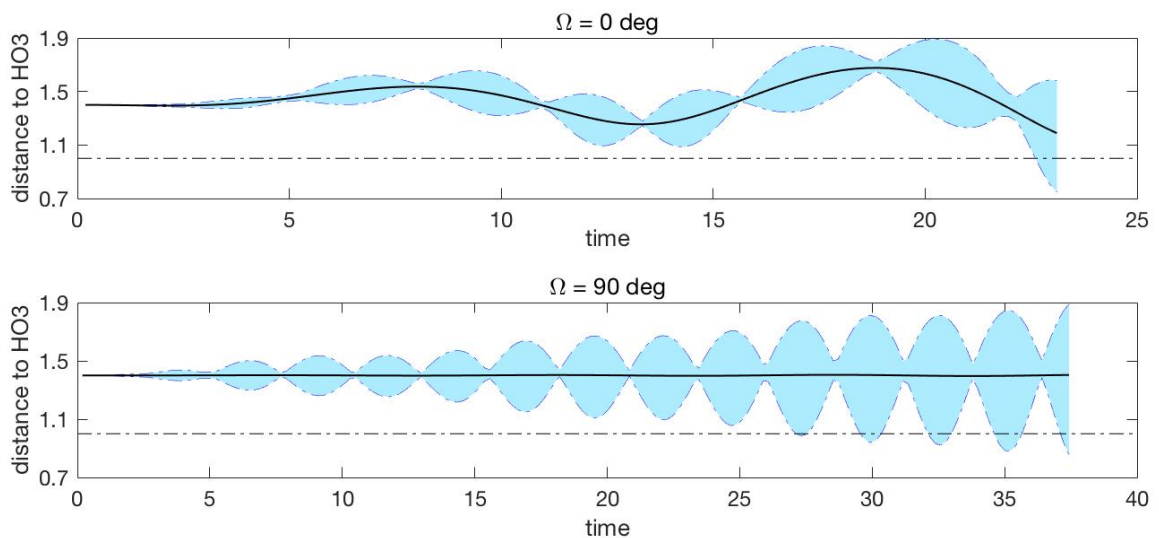


Figure 14 Evolution of the distance of center trajectories (black line) to HO3 and their bounds to HO3 (blue area) for $a = 1.4$, till the first split time epoch of each orbit.

5 Conclusions

By applying ADS algorithm, the uncertainties of central gravity and SRP are propagated along the orbital motion and their effects on orbits with different geometries are characterized. The map of the first split time indicates the dynamical structure of the system in terms of nonlinearity, robustness and practical stability. Polar orbits and terminator orbits are found to have strong robustness, which are validated by numerical integrations. They are good candidate of real mission orbits. In addition, it is also proven that robust orbits still exist even for very small bodies with very weak gravity. Therefore, though there is no direct correlation between the nonlinearity and the stability of the dynamics, the first split time and the number of splits for a fixed time duration can still be used as the indicator to identify regions of the motion staying within the required bounds, which can be recognized practical stability. In addition, the split history and bounds of the trajectory are evaluated for the sample polar orbits. The evolution of bounds provides quantitative information for designing robust navigation and control algorithms. In summary, this work contributes to systematically identifying the dynamical structure and robust regions of orbital motion near an asteroid considering model uncertainties. In future work, the uncertainty of the initial state and its effects on practical stability region should be investigated.

Acknowledgement

This work is supported by the Special Financial Grant of Chinese Postdoc Foundation and Natural Science Foundation of China for Young Scientist with No. 11703013. X. Hou wishes to thank the support from the Natural Science Foundation of China with No. 11773017.

References

- [1] S. Watanabe, Y. Tsuda, M. Yoshikawa, et al., Hayabusa2 Mission Overview, *Space Sci Rev*, 2017, 208: 3–16.
- [2] D. Loretta, S. Balram-Knutson, E. Beshore, et al., OSIRIS-REx: Sample Return from Asteroid (101955) Bennu, *Space Sci Rev*, 2017, 212: 925–984.
- [3] A. Cheng, A. Rivkin, P. Michel, et al., DART asteroid deflection test: Planetary defense and science objectives, *Planetary and Space Science*, 2018, 157: 104-115.
- [4] A. Pellacani, M. Graziano, M. Fittock, et al., HERA vision based GNC and autonomy, 8th European Conference for Aeronautics and Space Sciences (EUCASS), 2019.
- [5] X. Zhang, J. Huang, T. Wang, Z. Huo, ZhengHe – A Mission to a Near-Earth Asteroid and a Main Belt Comet (PDF). 50th Lunar and Planetary Science Conference, March, 2019.
- [6] C. Fuente Marcos, R. Fuente Marcos, Asteroid (469219) 2016 HO₃, the smallest and closest Earth quasi-satellite, *Monthly Notices of the Royal Astronomical Society*, 2016, 462(4): 3441-3456.
- [7] V. Arnold, *Mathematical Methods of Classical Mechanics*. Springer, 2nd edition, 1989.
- [8] S. Maybeck, *Stochastic Models, Estimation and Control*, Academic press, New York (1982).
- [9] S. Julier, J. Uhlmann, H. Durrant-Whyte, A new approach for filtering nonlinear systems, in: *Proceedings of IEEE American Control Conference*, 1995, 1628–1632.
- [10] G. Terejanu, P. Singla, T. Singh, P.D. Scott, Uncertainty propagation for nonlinear dynamic systems using gaussian mixture models, *Journal of Guidance, Control and Dynamics*, 2008, 31(6): 1623–1633.
- [11] N. Wiener, The homogeneous chaos, *Am. J. Math.* 1938, 60(4): 897–936.
- [12] M. Vasile, C. Absil, A. Riccardi, Set propagation in dynamical systems with generalised polynomial algebra and its computational complexity, *Commun Nonlinear Sci Numer Simulat*, 2019, 75: 22–49.
- [13] M. Berz, *Modern Map Methods in Particle Beam Physics*, Academic Press, New York, 1999: 82–96.
- [14] R. Armellin, P. Di Lizia, F. Bernelli-Zazzera, M. Berz, Asteroid close encounters characterization using differential algebra: the case of Apophis, *Celest. Mech. Dyn. Astron.*, 2010, 107(4): 451-470.

- [15] R. Armellin, P. Di Lizia, F. Bernelli-Zazzera, A high order method for orbital conjunctions analysis: sensitivity to initial uncertainties, *Advances in Space Research*, 2014, 53(3): 490–508.
- [16] D. Scheeres, *Orbital Motion in Strongly Perturbed Environments: Applications to Asteroid, Comet and Planetary Satellite Orbiters*. Springer-Praxis, London (UK), 2012.
- [17] J. Melman, E. Mooij, R. Noomen, State propagation in an uncertain asteroid gravity field, *Acta Astronautica*, 2013, 91: 8–19.
- [18] D. Scheeres, *Orbital Motion in Strongly Perturbed Environments: Applications to Asteroid, Comet and Planetary Satellite Orbiters*. Springer-Praxis, London (UK), 2012.
- [19] S. Hesar, D. Scheeres, J. McMahon, Sensitivity analysis of the OSIRIS-REx terminator orbits to maneuver errors, *Journal of Guidance, Control and Dynamics*, 2017, 40: 1–15.
- [20] J. Feng, R. Armellin, X. Hou, Orbit propagation in irregular and uncertain gravity field using differential algebra, *Acta Astronautica*, 2019, 161: 338-347.
- [21] A. Wittig, P. Di Lizia, F. Bernelli-Zazzera, et. al, Propagation of large uncertainty sets in orbital dynamics by automatic domain splitting, *Celestial Mechanics and Dynamical Astronomy*, 2015, 122(3): 239-261.
- [22] Cl. Froeschle, The Lyapunov characteristic exponents-applications to celestial mechanics. *Celestial Mechanics and Dynamical Astronomy*, 1984, 34: 95–115.
- [23] Haller, G. Distinguished material surfaces and coherent structures in three-dimensional fluid flows. *Physica D*, 2001, 149: 248-277.
- [24] W. Jin, F. Li, J. Yan, et al., Simulation of global GM estimate of Asteroid (469219) 2016 HO3 for China's future asteroid mission, *EPSC-DPS Joint Meeting*, 2019, 13: 15-20.
- [25] H. Hussmann, J. Oberst, K. Wickhusen, et. al, Stability and evolution of orbits around the binary asteroid 175706 (1996 FG3): Implications for the MarcoPolo-R mission, *Planetary and Space Science*, 2012, 70(1): 102-113.
- [26] J. Feng, X. Hou, Secular dynamics around small bodies with solar radiation pressure, *Commun Nonlinear Sci Numer Simulat*, 2019, 76: 71–91.